

Eccentric compressive behavior of novel composite walls with T-section

Ying Qin^{*1,2}, Xin Chen², Wang Xi², Xingyu Zhu² and Yuanze Chen²

¹Key Laboratory of Concrete and Prestressed Concrete Structures of Ministry of Education, Southeast University, Nanjing, China

²School of Civil Engineering, Southeast University, Nanjing, China

(Received January 15, 2020, Revised May 4, 2020, Accepted May 11, 2020)

Abstract. Double skin composite walls are alternatives to concrete walls to resist gravity load in structures. The composite action between steel faceplates and concrete core largely depends on the internal mechanical connectors. This paper investigates the structural behavior of novel composite wall system with T section and under combined compressive force and bending moment. The truss connectors are used to bond the steel faceplates to concrete core. Four short specimens were designed and tested under eccentric compression. The influences of the thickness of steel faceplates, the truss spacing, and the thickness of web wall were discussed based on the test results. The N - M interaction curves by AISC 360, Eurocode 4, and CECS 159 were compared with the test data. It was found that AISC 360 provided the most reasonable predictions.

Keywords: composite wall; eccentric compressive loading; experimental behavior; T-shaped section; truss connector

1. Introduction

Concrete walls are conventionally used as the vertical components to resist gravity load in structural systems (Beiraghi 2018, Bafti *et al.* 2019, Keihani *et al.* 2019, Yuksel *et al.* 2019). However, the walls at lower stories of high-rise buildings are normally designed to be very thick. In addition, the reinforcements in the walls are complicated and need large labor work. Meanwhile, steel plate shear walls are used to provide lateral resistance (Liu *et al.* 2018, Seddighi *et al.* 2019, Shariati *et al.* 2019, Curkovic *et al.* 2019, Deng *et al.* 2019), but their ability to resist gravity load is weak. To solve the problems mentioned above, double skin composite walls were introduced in recent years.

Double skin composite walls are constructed by two external steel faceplates and infilled concrete core. The composite effect between the two materials is achieved by using mechanical connectors such as shear studs (Yan *et al.* 2018), threaded rods (Prabha *et al.* 2013, Hossain *et al.* 2015), J-hook (Huang and Liew 2016), C-channel connectors (Yan *et al.* 2019), and embedded cold-formed steel tubes (Hilo *et al.* 2016). During the construction stage, the steel faceplates are used as the permanent formwork for pouring concrete. During the service stage, the steel faceplates can be considered as reinforcement of concrete. The concrete prevents the local buckling of steel faceplates and improves the behavior of steel faceplates, while the steel faceplates put the concrete core under tri-axial compression and enhances the compressive strength of concrete.

The research on seismic behavior of double skin composite walls has included that of Eom *et al.* (2009), Nie *et al.* (2013), Chen *et al.* (2015), Nguyen and Whittaker (2017), Ji *et al.* (2017), Huang *et al.* (2018), Chen *et al.* (2019), and Ma *et al.* (2019). Eom *et al.* (2009) performed cyclic tests on isolated and coupled double skin composite walls with rectangular and T-shaped sections to investigate their seismic behavior. Nie *et al.* (2013) tested a new type of double skin composite wall with vertical diaphragms and distributed batten plates under reversed cyclic lateral loading. Huang *et al.* (2018) extended the research by Nie *et al.* (2013) to use additional transverse stiffeners as mechanical connectors. The influences of axial force ratio, shear span ratio on the seismic behavior of the wall were evaluated. Chen *et al.* (2015) and Ma *et al.* (2019) tested isolated and coupled double skin composite wall with high-strength concrete and under cyclic lateral loading. The failure modes of all specimens were found to be dominated by flexural deformation. Nguyen and Whittaker (2017) used ABAQUS to predict the nonlinear cyclic behavior of double skin composite wall. It was found that the steel faceplates contributed 20%~70% of the entire shear resistance of the composite wall. Ji *et al.* (2017) present the experimental and numerical results of in-plane shear behavior of double skin composite walls with varied reinforcement ratios and axial force ratios. Vertical stiffeners and tie battens were found to increase the shear deformation capacity. In addition, the high reinforcement ratios and high axial force ratios were considered to contribute to potential crushing of concrete prior to yielding of steel faceplates. Meanwhile, several research has been conducted on the out-of-plane flexural behavior (Sener *et al.* 2015), deformation capacity (Hu *et al.* 2014), fire resistance (Wei *et al.* 2019), and blast resistance (Bruhl and Varma 2018).

As the component to resist gravity load in buildings and nuclear facilities, the compressive behavior of double skin composite wall is essential to the structural performance.

*Corresponding author, Associate Professor
E-mail: qinying@seu.edu.cn

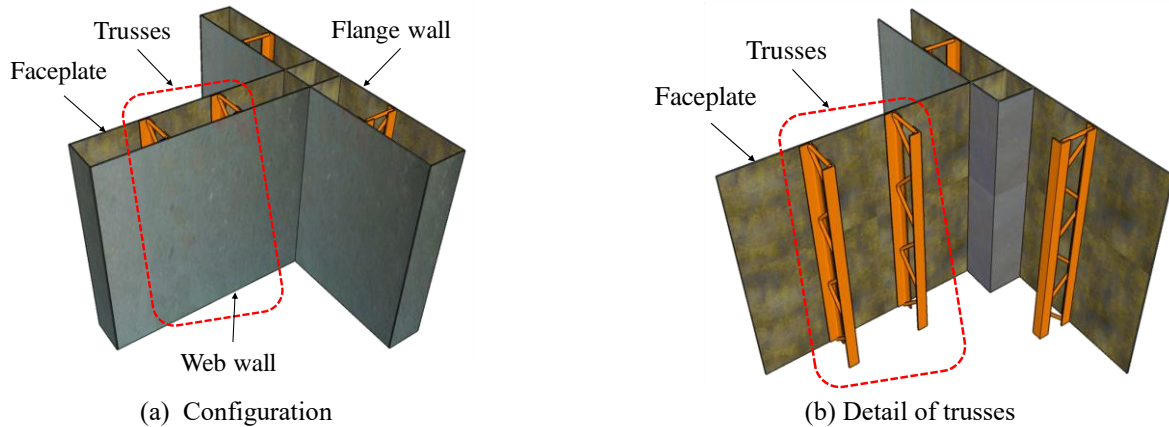


Fig. 1 Novel double skin composite wall with T-section (Qin *et al.* 2020)

Prabha *et al.* (2013) performed compressive tests on small-scaled profiled double skin composite walls with light weight foamed concrete. It was found that the axial resistance was largely affected by the confinement offered by shear studs and edge conditions. Zhang *et al.* (2014) studied the effect of shear connector design on the composite action and development length of steel faceplates in double skin composite walls. Hilo *et al.* (2016) presented the finite element model to simulate the axial behavior of profiled double skin composite walls. Parametric study was conducted to evaluate the effect of the thickness, number, and shape of embedded cold-formed steel tubes on the load resistance of the wall. Yang *et al.* (2016) investigated the influences of the arrangement of shear studs and the ratio of connector spacing and steel faceplate thickness on the buckling behavior of double skin composite walls. Huang and Liew (2016) proposed the configuration of double skin composite wall with J-hook connectors. The compression tests showed that the J-hook connectors were essential to provide the composite action and prevent the premature local buckling of steel faceplates.

From literature review it can be found that, most research about the compressive behavior of double skin composite wall focused on rectangular section. When applied in building system and nuclear construction, double skin composite wall should meet requirement for different layout plans such as T section, L section and cruciform section. Therefore, the design of double skin composite wall should consider varied cross-section shapes for engineering application.

This paper investigates the structural behavior of a novel double skin composite wall system with T section and under eccentric compression. This wall system was proposed by Qin *et al.* (2019) and the compressive behavior of the wall with rectangular section has been investigated. Meanwhile, the eccentric compressive performance of T-shaped wall with the height of 3000 mm has been studied by Qin *et al.* (2020). Compared to high walls with the global buckling of web wall as investigated by Qin *et al.* (2020), short wall in this research will fail by strength. Furthermore, the T-shaped walls in Qin *et al.* (2020) used ready-to-use tubes to enhance all boundaries of the wall. There is a need to

evaluate the wall system without boundary column. As will be seen from the analysis in this paper, the strength of the wall which is not designed with boundary elements would be lower. Fig. 1 shows the configuration of the studied wall. The wall is composed of two external steel faceplates and infilled concrete. Steel trusses are used to connect the two external steel faceplates. The steel truss, which is welded to the internal surface of steel faceplates by automatic machine, is constructed by two angles serving as chord members and curl rebar serving as web member. The truss connectors prevent tensile separation between the steel faceplates and the concrete core and also offer the necessary shear resistance when the double skin composite wall is under eccentric compression. Ready-to-use tube is used to the intersection part between the web wall and the flange wall, while the channel sections is used to connect the two separate steel faceplates by complete joint penetration weld along the wall height.

2. Experimental program

2.1 Test specimens

Four double skin composite wall specimens were designed and tested under eccentric compression, as shown in Fig. 2 and Table 1. It should be noted that Side N, Side S, Side W, and Side E in Fig. 2 are used to mark the four sides of the wall. The test variables were the thickness of steel faceplate, the truss spacing, and the thickness of web wall. Specimen CW1 was designed as the benchmark. The height of the specimen was 500 mm, the width of the web wall and the flange wall were 750 mm and 450 mm, respectively, and the thickness of the web wall and the flange wall were both 150 mm. The steel faceplates had the thickness of 4 mm. The angles used to form the chord members of truss connectors had the cross section of L40×40×4 mm, and the curl rebar used to form the web member of truss connectors had the diameter of 8 mm. The truss spacing was designed as 200 mm, and the corresponding ratio between the truss spacing and steel faceplate thickness was $50\sqrt{235/f_y}$. The

flange width of the channel sections which were used to bond the external steel faceplates was 50 mm. Specimen CW2 was designed with different steel faceplate thickness of 6 mm. Specimen CW3 were used to evaluate the influence of truss spacing. The truss spacing of Specimen CW3 was 300 mm, and the ratio between truss spacing and faceplate thickness was $75\sqrt{235/f_y}$. For Specimen CW4, 30 mm wider web wall was used to consider the effect of web wall width.

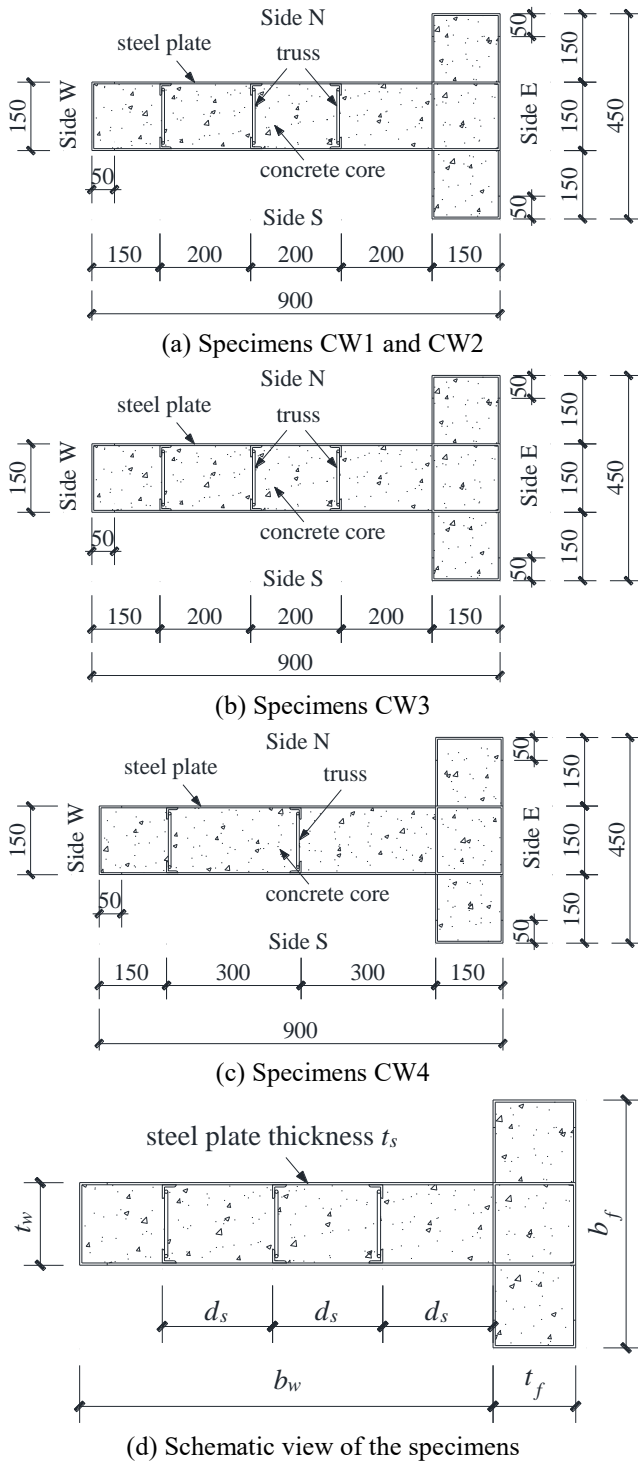


Fig. 2 Details of test specimens (dimension: mm)

Table 1 Specimen details

Specimen No.	h	b_w	t_w	b_f	t_f	t_s	d_s
	mm	mm	mm	mm	mm	mm	mm
CW1	500	750	150	450	150	4	200
CW2	500	750	150	450	150	6	200
CW3	500	750	150	450	150	4	300
CW4	500	750	180	480	150	4	200

Note: h is the height of the wall, b_w and t_w are the width and thickness of web wall, respectively; b_f and t_f are the width and thickness of flange wall, respectively; t_s is the thickness of steel faceplate; and d_s is the truss spacing

2.2 Material properties

Three tensile coupons were cut from the original batch of steel plate to determine the material property of steel. The dimensions of the coupons were designed based on the requirement incorporated in GB/T 2957-2018 (2018) Steel and steel products-Location and preparation of samples and test pieces for mechanical testing. The average yield strength, ultimate strength, and modulus of elasticity for 4 mm steel plate were 346.0 MPa, 364.8 MPa, and 1.99×10^5 MPa, respectively. For steel plate with the thickness of 6 mm, the average yield strength, ultimate strength, and modulus of elasticity were 227 MPa, 378 MPa, and 2.02×10^5 MPa, respectively.

In order to obtain the compressive strength of concrete core, three cubes with the dimension of 150 mm \times 150 mm \times 150 mm were cast the cured. The cubes were tested based on GB/T 50081-2019 (2019) Standard for test methods of concrete physical and mechanical properties. The average cubic compressive strength f_{cu} was 23.9 MPa. According to GB 50010-2010 (2015) Code for design of concrete structures, the corresponding cylinder compressive strength f_c can be calculated by Eq. (1).

$$f_c = 0.88\alpha_1\alpha_2f_{cu} \quad (1)$$

where α_1 is the factor to consider the difference between cylinder compressive strength and cubic compressive strength and can be taken as 0.76, and α_2 is the factor to consider the reduction due to brittle characteristics and can be taken as 1.0.

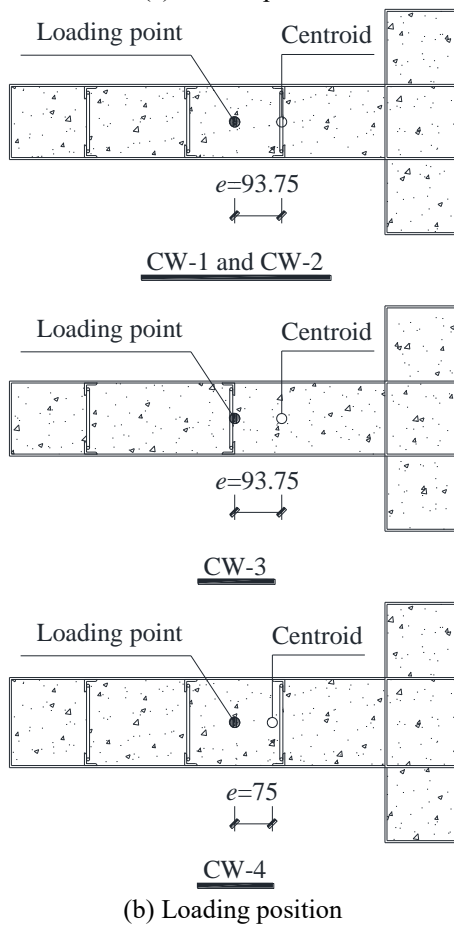
2.3 Test setup and loading procedure

The test specimens were placed in the loading machine with the loading capacity of 10000 kN at Southeast University, as shown in Fig. 3(a). Fine sand was paved at the top of the specimens to ensure the tested wall was in close contact with the test rig, which guaranteed the compression was applied to the entire cross section of the wall. The eccentric compression in the wall led to combined axial compression and bending moment, as shown in Fig. 3(b). The tests were performed in a load-controlled manner with the load intervals of 500 kN to failure where the load decreased to 85% of peak load or the separation occurred

between the web wall and the test rig due to the large uneven deformation under eccentric compression, whichever is earlier.



(a) On-site photo



(b) Loading position

Fig. 3 Test setup (dimension: mm)

2.4 Instrumentations

Ten displacement transducers were used to monitor the deformation of the tested walls, as shown in Fig. 4. Four displacement transducers (D1~D4) were mounted vertically, with their measuring heads attaching to the bottom of the wall, to obtain the axial shortening of the specimens. Another six displacement transducers (D5~D10) were placed horizontally to record the out-of-plane deformation. Eighteen and nineteen strain gauges, respectively, were used for Specimen CW-3 and the other three specimens. The strain gauges were arranged at the mid-height cross-section to determine the vertical and lateral strains, as shown in Fig. 5.

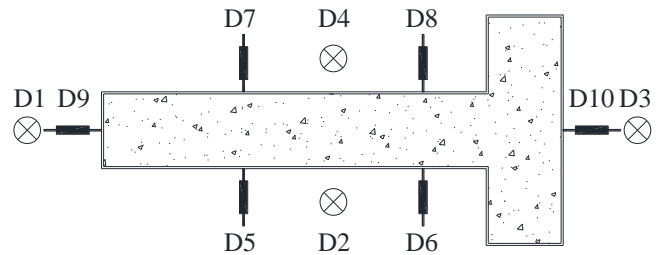
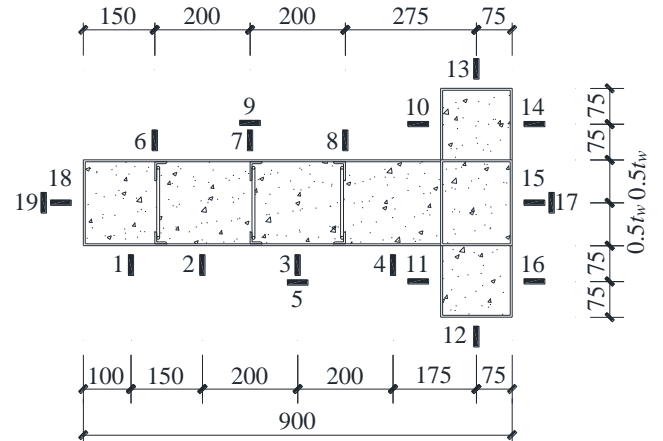
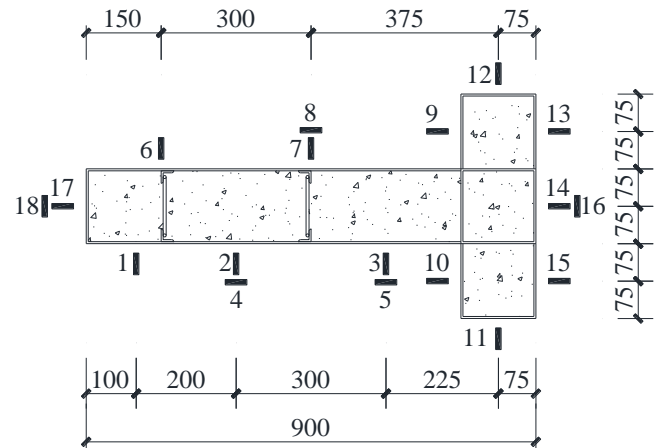


Fig. 4 Placement of displacement transducers



(a) Specimens CW-1, CW-2, and CW-4



(b) Specimen CW-3

Fig. 5 Placement of strain gauges (dimension: mm)

3. Test results

3.1 Failure modes

All test specimens failed by local buckling of the web wall, followed by the crushing of concrete. No obvious deformation or damage were found on the flange wall. Comparing to Specimen CW1, the local buckling occurred in Specimens CW2, CW3, and CW4 at higher, lower, and comparable loading level, respectively. This indicated that the thicker steel faceplates prevent the premature local buckling, while the larger truss spacing in walls weakens the restraint to the steel faceplates and thus the steel faceplates are more vulnerable to buckling. Meanwhile, the influence of width-to-thickness ratio on buckling behavior seems to be insignificant.

Specimen CW1 behaved in a smooth manner. No apparent deformation was observed during the early stage of loading. Slight local buckling was found on side S of web wall when the load reached 3500 kN. The buckling became more severe as the load continued to increase. The steel faceplate of web wall on side N started to buckle at the loading level of 5000 kN. Meanwhile, the web wall on side W bulged out at the top. The specimen finally reached its ultimate capacity of 5300 kN. The corresponding bending moment, which is calculated by multiplying the compressive force by the eccentricity, was 497 kN·m. The failure mode of Specimen CW1 was shown in Figs. 6(a) and 6(b).

During the testing of Specimen CW2, no obvious physical observation was noticed until the load reached 6000 kN, when slight sound was heard but no noticeable buckling was observed. The web wall on sides N, S, and W suddenly buckled outward near the top of wall at the loading level of 7000 kN, as shown in Figs. 6(c) and 6(d). The ultimate capacity was 7480 kN with the bending moment of 701 kN·m.

For Specimen CW3, local buckling occurred on side N of web wall at an early loading level of 2500 kN. As the load progressed to 3500 kN, the web wall on side W slightly buckled. The buckling on side N of web wall became more obvious when the load reached 4000 kN, as shown in Fig. 6(e), which was accompanied by clear sound from the specimen. When the specimen arrived at its ultimate capacity of 4500 kN, the web wall on side S bulged out at the top, as shown in Fig. 6(f). The corresponding bending moment was 422 kN·m.

Specimen CW4 showed similar structural performance to Specimen CW1 at the beginning of the test. The axial shortening stably went up with the increase in eccentric compression. The web wall on side W started to bulged out when the compressive load arrived at 3000 kN. As the load increased to 4000 kN, continuous sound was emitted from the specimen, which was believed to be caused by deformation of steel faceplates. The local buckling of web wall on side N was found close to the top of wall at the loading level of 4500 kN. Similar buckling was observed at the bottom of web wall on side N when the load reached 5500 kN, as shown in Fig. 6(g). Simultaneously, the web wall on side S was noticed to deform outward, as shown in

Fig. 6(h). The ultimate capacity of the specimen was 5760 kN, and the resulted bending moment was 432 kN·m.



(a) Specimen CW1 (Side S)



(b) Specimen CW1 (side N)



(c) Specimen CW2 (side S)



(d) Specimen CW2 (side N)

Continued-



(e) Specimen CW3 (side N)



(f) Specimen CW3 (side S)



(g) Specimen CW4 (side N)



(h) Specimen CW4 (side S)

Fig. 6 Failure modes

3.2 Load-axial displacement responses

The relationships between compressive load and axial

displacement for all specimens are illustrated in Fig. 7. It can be observed that all specimens showed similar structural behavior under eccentric compression. During the first stage, the specimens behave in the elastic range. The curves steadily go up with the growth in loading in a linear manner. In the second stage, local buckling occurs and plastic deformation accumulates in the specimens. The slopes of the curves gradually decrease until reaching the ultimate capacity. The third stage starts from the peak load point to the failure point. The specimens experience severe local buckling of steel faceplates and crushing of concrete core and are not able to sustain their resistance. The curves start to climb down to the failure.

Table 1 lists the ultimate compression N_u and the corresponding bending moment M_u . It can be seen that the increase in steel faceplate thickness is effective in improving the structural behavior of the wall. The increase of steel faceplate thickness from 4 mm in Specimen CW1 to 6 mm in Specimen CW2 leads to 41% higher resistance. Meanwhile, the axial displacement corresponding to the ultimate resistance is decreased by 19.6%. It means specimen with thicker steel faceplates owns larger ultimate resistance and smaller deformation. This is attributed to the fact that local buckling is postponed in thicker steel faceplate. In addition, the comparison between Specimens CW1 and CW3 shows that the truss spacing has significant influence on the ultimate resistance. The resistance of wall is decreased by 15.1% when the truss spacing increases from 200 mm to 300 mm (Table 1 and Fig. 2). This indicates that smaller truss spacing offers stronger restraint to steel faceplate and enhances the composite action between the steel faceplate and concrete core.

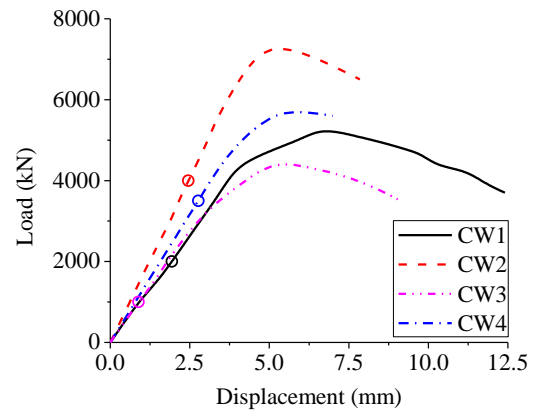


Fig. 7 Load versus axial displacement curves

Table 1 Test results

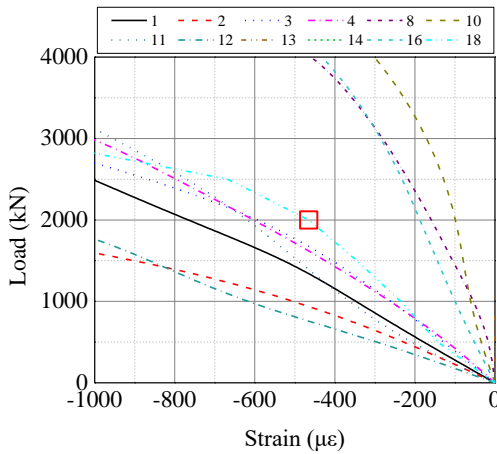
Specimen No.	N_b	δ_b	N_u	δ_u	M_u	$\frac{N_b}{N_u}$
	kN	mm	kN	mm	kN·m	
CW1	2000	1.94	5300	6.63	497	0.38
CW2	4000	2.45	7480	5.33	701	0.53
CW3	1000	0.89	4500	5.19	422	0.22
CW4	3500	2.77	5760	5.63	432	0.61

3.3 Buckling stress

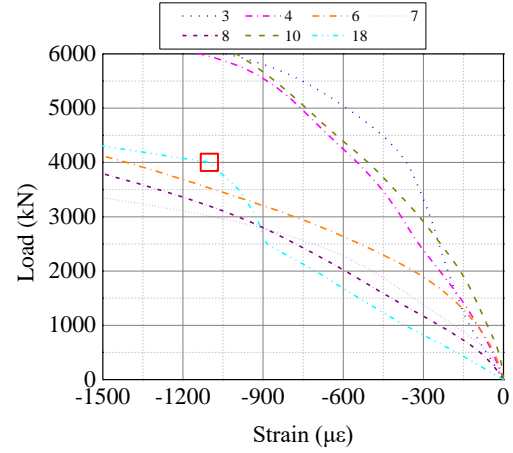
For double skin composite wall subjected to eccentric compression, the thin steel faceplates would buckle when the load reaches the critical buckling load. Due to the restraint offered by concrete core and truss connectors, the steel faceplate can only deform outward. The strain at the buckling location changes obviously when local buckling occurs. This can be used to identify the buckling strain and the corresponding buckling load.

Fig. 8 shows the partially-enlarged drawing of load-strain curves for several strain gauges (Fig. 5). The point where strain changes significantly was considered as the buckling point and marked by red square. As can be seen from Fig. 8(a), Specimen CW1 has a buckling strain of $465 \mu\epsilon$, and the corresponding buckling stress and buckling load are 92.5 MPa and 2000 kN . Fig. 8(b) shows that Specimen CW2 has a buckling strain of $1101 \mu\epsilon$, and the corresponding buckling stress and buckling load are 222.4 MPa and 4000 kN . It can be noticed from Fig. 8(c) that Specimen CW3 has a buckling strain of $180 \mu\epsilon$, and the corresponding buckling stress and buckling load are 35.8 MPa and 1000 kN . Fig. 8(d) indicates that Specimen CW4 has a buckling strain of $420 \mu\epsilon$, and the corresponding buckling stress and buckling load are 83.6 MPa and 3500 kN .

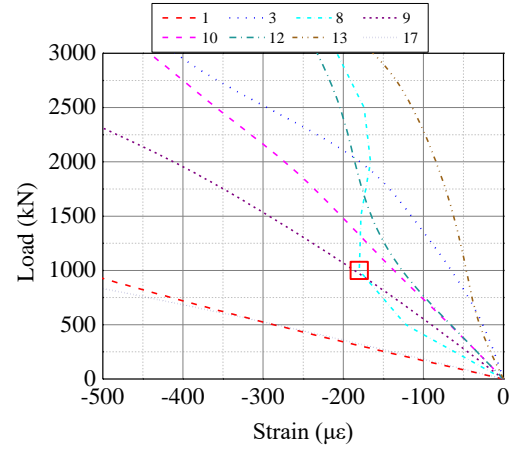
The buckling load N_b and the corresponding axial displacement δ_b for each specimen were given in Table 1. The buckling loads were also labelled in Fig. 7 by circles. It can be observed from Fig. 7 that the slope of curves shows no noticeable change after buckling occurs. This indicates that the stiffness of the wall is not significantly affected by the local buckling of steel faceplate. As can be seen from Table 1, the ratios of buckling load to ultimate load range from 0.22 to 0.61. Specimen CW3 has the lowest N_b/N_u ratio of 0.22, which means the increase in truss spacing leads to premature local buckling. Meanwhile, Specimens CW2 and CW4 own greater N_b/N_u ratio comparing with Specimen CW1. This indicates that the increase in steel faceplates thickness or web wall thickness delays the occurrence of local buckling.



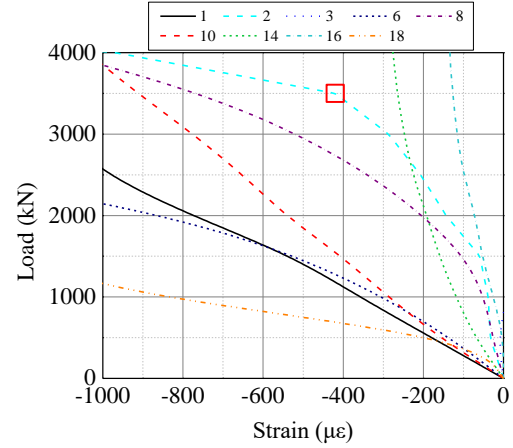
(a) Specimen CW1
Continued-



(b) Specimen CW2



(c) Specimen CW3



(d) Specimen CW4

Fig. 8 Determination of buckling strain

3.4 Boundary condition of steel faceplate

The steel faceplate in double skin composite wall is in rigid contact with concrete core. Meanwhile, it is restrained by surrounded truss connectors and adjacent plates. The degree of restraint to steel faceplate is largely dependent on the stiffness of these components. For steel faceplate in composite structures under eccentric compression, the critical local buckling stress $\sigma_{cr,Euler}$ can be calculated by

Eq. (2) (Qin *et al.* 2018).

$$\sigma_{cr,Euler} = \frac{\pi^2 E_s}{12k_{cr}^2 (d_s/t_s)^2} \quad (2)$$

where $k_{cr} = \frac{k}{1-0.5\zeta}$ is the critical local buckling coefficient for steel faceplate under eccentric compression; E_s is the elastic modulus of steel faceplate; k is the critical local buckling coefficient for steel faceplate under axial compression; ζ is the loading stress gradient parameter due to eccentric compression. It can be calculated that the values of ζ are 0.033621 for Specimens CW1 and CW2, 0.074743 for Specimen CW3, and 0.02917 for Specimen CW4. Rearranging Eq. (2) gives the normalized buckling strain $\varepsilon_{cr}/\varepsilon_y$ as the function of the normalized slenderness ratio $d_s/t_s \times \sqrt{f_y/E_s}$,

$$\varepsilon_{cr}/\varepsilon_y = \frac{\pi^2}{12k_{cr}^2} \cdot \frac{1}{\left(d_s/t_s \times \sqrt{f_y/E_s}\right)^2} \quad (3)$$

The relationships between the normalized buckling strain $\varepsilon_{cr}/\varepsilon_y$ and the normalized slenderness ratio $d_s/t_s \times \sqrt{f_y/E_s}$ for all specimens were plotted in Fig. 9. The Euler curves with $k=0.7$ and $k=1.0$ were also plotted for each case. It can be seen that in general, all test data were lying between the two Euler curves. It means that the boundary condition for steel faceplates in double skin composite walls is more appropriate to be assumed as elastically restrained, which is weaker than clamped and stronger than simple supported. It can also be found from Fig. 9(a) that the data for Specimen CW1 is closer to Euler curve with $k=0.7$ than Specimen CW2. This is because the truss connectors with the same configuration provide relatively better confinement to thin steel faceplate. The comparison between Specimens CW1 and CW3 shows that the confinement to steel faceplates in Specimen CW3 is weaker than in Specimen CW1. This is reasonable because the increase in truss spacing weakens the restraint of truss connector to steel faceplate.

3.5 Axial stiffness

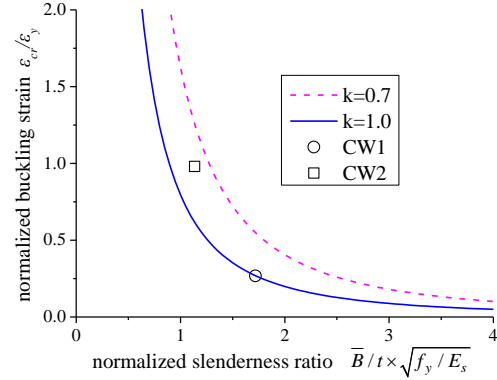
The initial stiffness K_i of all specimens are given in Table 2. It can be seen that the initial stiffness increases with the growth in either steel faceplate thickness or web wall thickness, while decreases as the truss spacing becomes larger.

In order to further quantify the influence of local buckling on the axial stiffness, two types of secant stiffness were used. The first one K_b takes the point corresponding to buckling load as the starting point and the point corresponding to $0.8N_u$ as the ending point, and the second one $K_{0.3u}$ takes the point corresponding to $0.3N_u$ as the starting point and the point corresponding to $0.8N_u$ as the ending point. The calculated K_b and $K_{0.3u}$ are shown in Table 2. It can be noticed that the two kinds of secant stiffness exhibit no obvious differences. This directly demonstrates

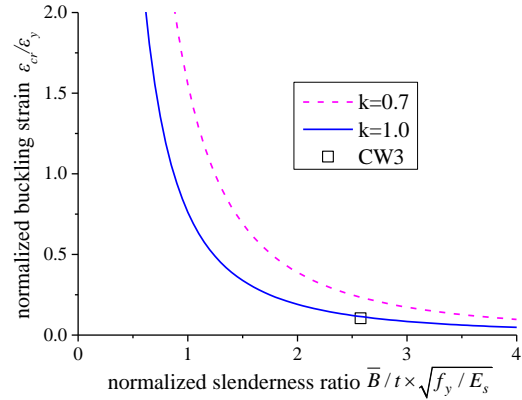
that the influence of local buckling on axial stiffness is negligible.

3.6 Ductility

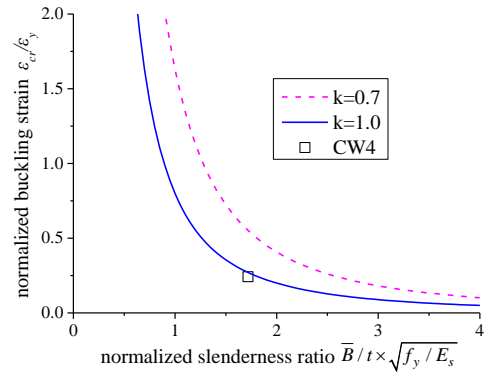
The ductility ratio μ is used to evaluate the ability of double skin composite walls to undergo significant plastic deformation without severe strength deterioration.



(a) Specimens CW1 and CW2 ($\zeta=0.033621$)



(b) Specimen CW3 ($\zeta=0.074743$)



(c) Specimen CW4 ($\zeta=0.02917$)

Fig. 9 Comparison with Euler curves

Table 2 Axial stiffness

Specimen	K_i	$0.3N_u$	$d_{0.3u}$	$0.8N_u$	$d_{0.8u}$	K_b	$K_{0.3u}$
	kN/mm	kN	mm	kN	mm	kN/mm	kN/mm
CW1	1136	1590	1.56	4080	3.76	1142	1129
CW2	1633	2244	1.39	5984	3.67	1634	1640
CW3	1124	1350	1.24	3600	3.56	974	971
CW4	1270	1728	1.00	4608	3.70	1186	1065

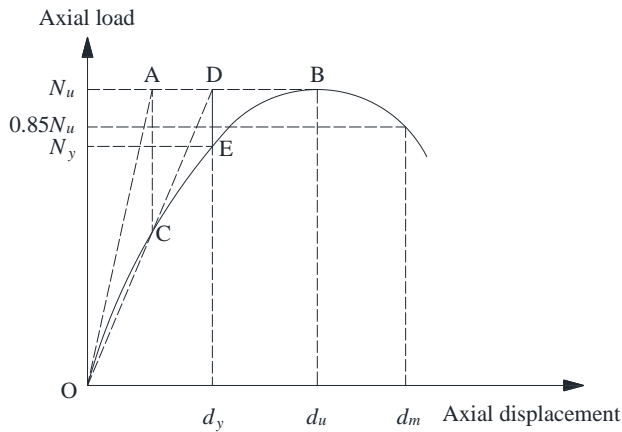


Fig. 10 Determination of yield displacement

It is defined as the ratio of the nominal maximum displacement (d_m) to the displacement corresponding to the yielding point (d_y), as given by Eq. (4) (Xiong *et al.* 2017), where the nominal maximum displacement is the greater value of the displacement corresponding to the failure point and the displacement corresponding to $0.85N_u$ during the descending stage. The yielding displacement d_y can be determined by the method shown in Fig. 10.

$$\mu = \frac{d_{0.85u}}{d_y} \quad (4)$$

The yielding load N_y , the yielding displacement d_y , and the calculated ductility ratios μ for four specimens are listed in Table 3. It can be seen that the increase in steel faceplate thickness, truss spacing, and web wall thickness leads to the reduction in ductility ratio.

Table 3 Ductility and strength index

Specimen	N_y	d_y	d_m	μ	N_f	SI
	kN	mm	mm		kN	
CW1	4900	5.53	10.57	1.91	5013	0.70
CW2	7180	4.84	7.85	1.62	6592	1.05
CW3	4200	4.65	8.31	1.79	5013	0.60
CW4	5500	4.94	7.01	1.42	5468	0.72

3.7 Strength index

The strength index SI is introduced to investigate the capacity utilization of double skin composite walls. It can be calculated by the ratio of the ultimate compression N_u in the test to the entire cross-sectional capacity under axial compression N_f , as expressed by Eq. (5).

$$SI = \frac{N_u}{N_f} = \frac{N_u}{f_y A_s + f_c A_c} \quad (5)$$

where A_s and A_c are the cross-sectional area of steel and concrete core, respectively.

The strength index for four specimens are provided in Table 3. The strength index increases as the steel faceplate thickness and web wall width increases, which reveals that the steel faceplate thickness and web wall width are effective to affect the loading resistance of the composite walls. The truss spacing also has influence on the strength index. The strength index decreases from 0.70 for Specimen CW1 to 0.60 for Specimen CW3.

3.8 Load versus out-of-plane lateral deformation responses

Fig. 11 shows the relationship between the compressive load and the out-of-plane lateral displacement. At the beginning of loading, the out-of-plane deformation is small. The deformation gradually develops as the local buckling starts to occur in the wall. After reaching the ultimate resistance, the out-of-plane deformation progresses more quickly. Meanwhile, it can be found that the values of W_{10} for each specimen are quite small, which means the out-of-plane deformation of flange wall is insignificant during the loading process. In most cases, the largest out-of-plane deformation appears at the side of web wall rather than at the edge. This is because the confinement to steel faceplate at the edge is stronger than that at the side.

The comparison among Specimens CW1, CW2, and CW4 shows that the out-of-plane deformation is largely reduced with the increase in steel faceplate thickness and web wall thickness. It can also be found from Fig. 11(c) that larger truss spacing increases the out-of-plane deformation due to weaker restraint to steel faceplate.

3.9 Load-strain responses

Fig. 12 shows the load versus strain curves for Specimen CW1. The load versus strain responses of the other three specimens are similar and thus, they are not presented herein.

It can be seen that in general, the strains slowly develop before the plastic deformation occurs. The strains increase more quickly after the buckling of steel faceplate. The increase rate becomes more rapid after the ultimate resistance has been reached.

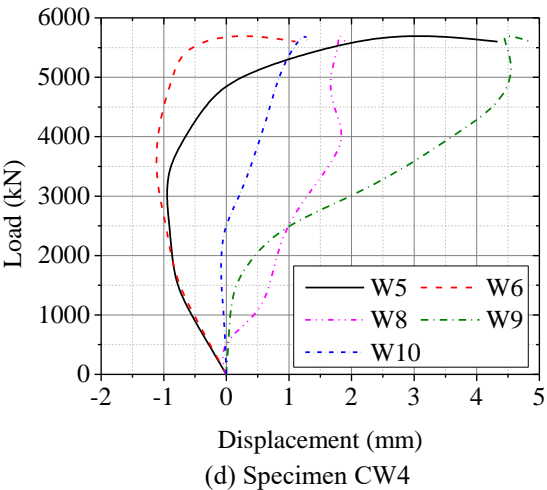
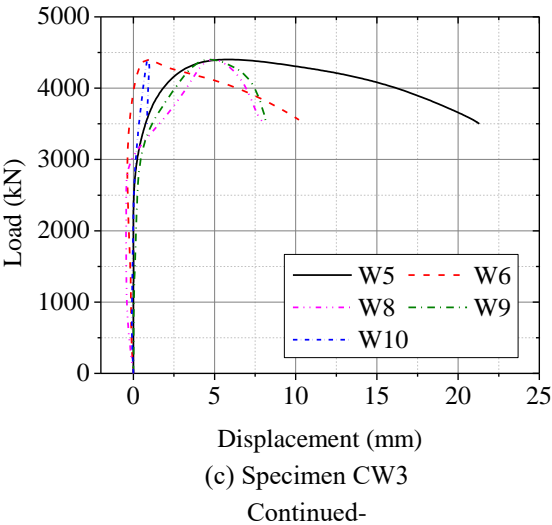
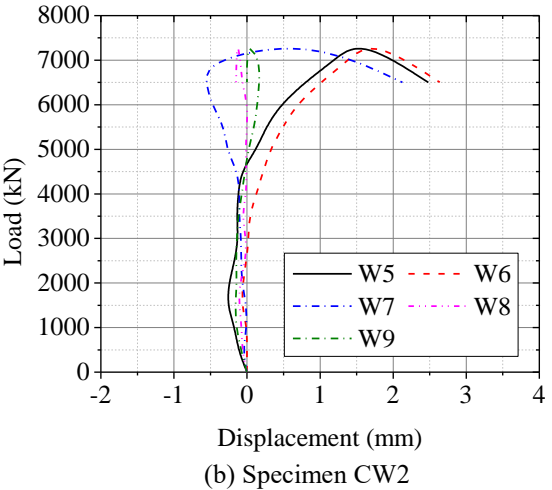
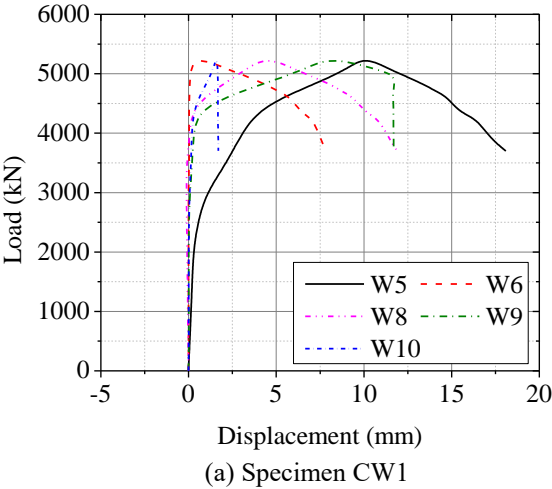


Fig. 11 Load-out-of-plane displacement curves

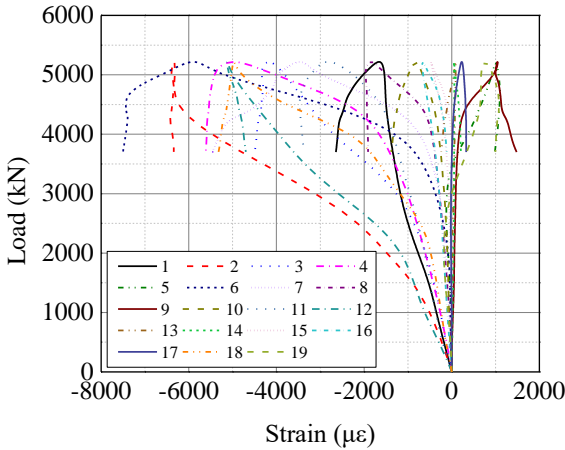
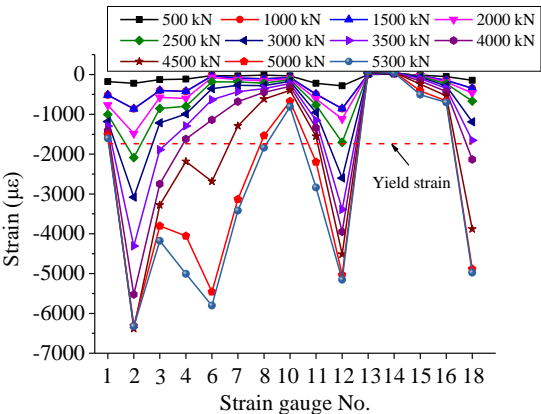


Fig. 12 Load-strain curves for Specimen CW1



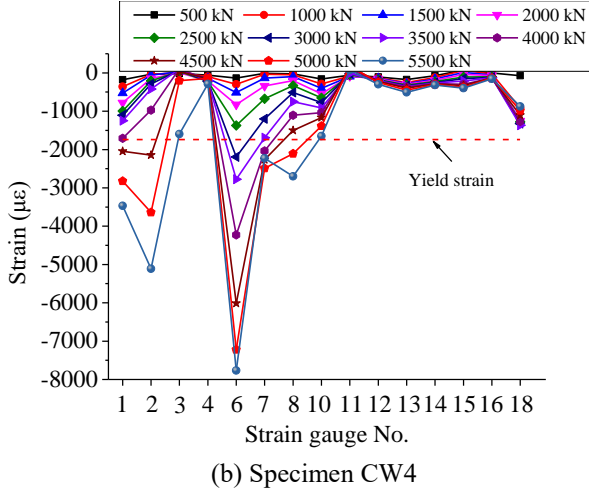


Fig. 13 Strain distribution based on loading levels

The strain distributions for Specimens CW1 and CW4 are given in Fig. 13. The yield strain was marked as red dashed line. It can be found that for the strain gauges at most locations, the strains increase as the distance from the neutral axis increases, which indicates the assumption planes remain plane can be applied to this type of wall. Meanwhile, more locations yield in Specimen CW1 than in Specimen CW4. This is because greater portion of load is carried by concrete in Specimen CW4 due to thicker web wall.

4. Design method

4.1 AISC 360-16

AISC 360-16 (2016) provides the method to calculate the resistance of singly symmetric concrete filled members subjected to combined bending moment and axial force, as shown in Eqs. (6).

When $\frac{N_u}{N_{um}} \geq 0.2$,

$$\frac{N_u}{N_{um}} + \frac{8M_u}{9M_{um}} \leq 1.0 \quad (6a)$$

When $\frac{N_u}{N_{um}} < 0.2$,

$$\frac{N_u}{2N_{um}} + \frac{M_u}{M_{um}} \leq 1.0 \quad (6b)$$

where N_u is the required axial strength; N_{um} is the available axial strength and can be calculated by Eq. (7) for double skin composite walls; M_u is the required bending moment; M_{um} is the available bending moment, which is the moment corresponding to plastic stress distribution over the composite cross section.

$$N_{um} = f_y A_s + 0.85 f_c A_c \quad (7)$$

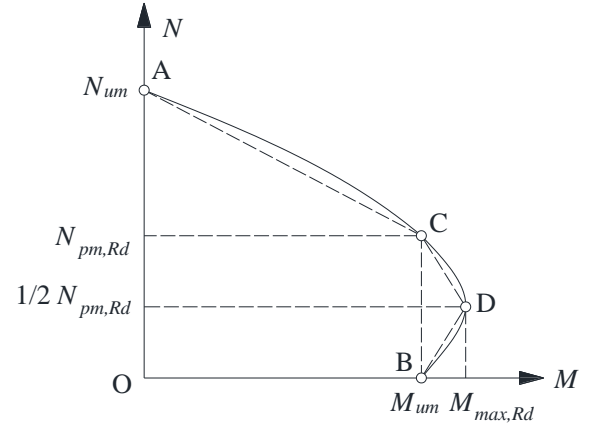


Fig. 14 Simplified interaction curve in Eurocode 4

4.2 Eurocode 4

Eurocode 4 (EN 1994-1-1:2004, 2004) used a polygonal diagram (the dashed line in Fig. 14) to replace the interaction curve (the solid line in Fig. 14) of composite structures under combined compression and bending, assuming rectangular stress blocks and neglecting the tensile strength of concrete.

At point A, the plastic resistance to compression N_{um} of the composite wall can be obtained by the summation of the plastic resistance of both steel and concrete, as given by Eq. (8).

$$N_{um} = f_y A_s + f_c A_c \quad (8)$$

At points B and C, M_{um} is the plastic bending moment under pure bending. $N_{pm,Rd}$ at point C should be taken as $f_c A_c$. $M_{max,Rd}$ at point D is the maximum plastic bending moment taking into account the compressive normal force $\frac{1}{2} N_{pm,Rd}$.

4.3 CECS 159:2004

CECS 159:2004 (2004) applied two straight lines to predict the sectional strength of composite structures under eccentric compression. The interaction curve between compressive force and bending is expressed by Eq. (9).

$$\frac{N_u}{N_{um}} + (1 - \alpha_c) \frac{M_u}{M_{um}} \leq 1.0 \quad (9a)$$

$$\frac{M_u}{M_{um}} \leq 1.0 \quad (9b)$$

where N_{um} can be calculated by Eq. (8); and α_c is the action factor for concrete core and can be determined by Eq. (10).

$$\alpha_c = \frac{f_c A_c}{f_y A_s + f_c A_c} \quad (10)$$

4.4 Determination of key parameters

In order to plot the interaction curves specified by three modern codes mentioned above, it is necessary to determine the values of some key parameters (i.e., M_{um} and $M_{max,Rd}$) appeared in Eqs. (6) and (9) and Fig. 14.

For double skin composite wall with T-section, the method to calculate the plastic bending moment proposed by Qin *et al.* (2020) was adopted in this research. The bending moment in different directions leads to different plastic stress distribution, due to the singly symmetric rather than doubly symmetric geometrical characteristics. The plastic stress distributions of the composite wall under combined compressive force and bending moment are illustrated in Fig. 15.

Force equilibrium should be satisfied in both cases. The equilibrium for compressive force and bending moment are given in Eqs. (11(a)) and (11(b)), respectively (Qin *et al.* 2020).

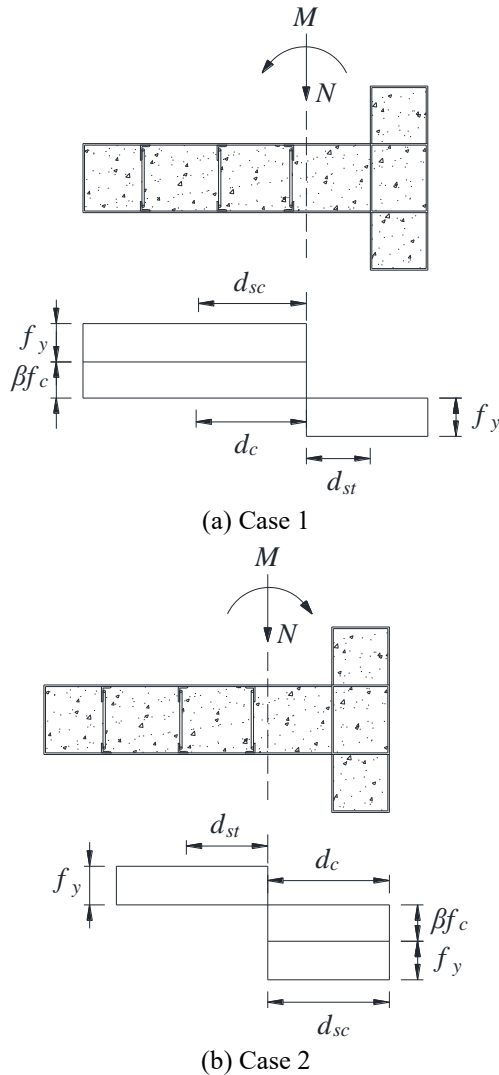


Fig. 15 Stress distribution diagram under eccentric compression (Qin *et al.* 2020)

$$N = f_c A_{cc} + f_y A_{sc} - f_y A_{st} \quad (11a)$$

$$M_{um} = f_c A_{cc} d_c + f_y A_{sc} d_{sc} + f_y A_{st} d_{st} \quad (11b)$$

where A_{cc} is the cross-sectional area of concrete under compression; A_{sc} and A_{st} are the cross-sectional area of steel faceplate under compression and tension, respectively; d_c is the distance between the neutral axis and the resultant of compressive force in the concrete; d_{sc} is the distance between the neutral axis and the resultant of compressive force in the steel; and d_{st} is the distance between the neutral axis and the resultant of tensile force in the steel.

Setting the value of N in Eq. (11(a)) to be $\frac{1}{2} N_{pm,Rd}$, the value of maximum plastic bending moment $M_{max,Rd}$ can be obtained from Eq. (11(b)). Similarly, the plastic bending moment M_{um} under pure bending can be calculated by setting N in Eq. (11(a)) to be zero.

4.5 Discussion

The test data and the N - M interaction curves predicted by AISC 360-16, Eurocode 4, and CECS 159:2004 are plotted in Figs. 16(a)-16(c). Basically, it can be observed that most the test data are outside the specified curve for AISC 360-16. It can also be found that Specimen CW3 with the truss spacing of 300 mm is inside the curve. This indicates that the ratio between the truss spacing and steel faceplate thickness should be limited to no greater than $50 \sqrt{235/f_y}$ if AISC 360-16 is applied to predict the wall strength. In contrast, both Eurocode 4 and CECS 159 provide overestimation for most specimens, which is on the unsafe side. This is due to the fact that these two codes consider the concrete could reach the compressive strength of f_c , which overestimates the actual compressive strength that concrete can be reached in the composite wall.

5. Conclusions

This paper experimentally and theoretically investigated the structural behavior of the novel T-shaped double skin composite walls under eccentric compression. Compressive tests were conducted on four specimens with varied faceplate thickness, truss spacing, and web wall thickness. The following conclusions are drawn based on the experimental and theoretical investigation.

(1) The failure mode of the tested walls initiated with the local buckling of web wall, followed by the concrete crushing. The flange wall showed no obvious damage or deformation.

(2) The boundary conditions of steel faceplates in composite walls are more appropriate to be considered as elastically restrained.

(3) Increasing faceplate thickness rather than web wall thickness is more effective in improving the resistance and stiffness of the composite wall. Larger truss spacing

weakens the restraint to steel faceplate and thus leads to the reduction in both resistance and stiffness.

(4) The ductility ratio decreases with the increase in faceplate thickness, truss spacing and web wall thickness. Meanwhile, the strength index increases with the growth in faceplate thickness and truss spacing while decreases with the increasing truss spacing.

(5) The test data were compared with the N - M interaction curves specified by three modern codes. It was found that the predictions by AISC 360-16 were the most reasonable, while Eurocode 4 and CECS 159 overestimated the actual resistance of the composite wall under eccentric compression.

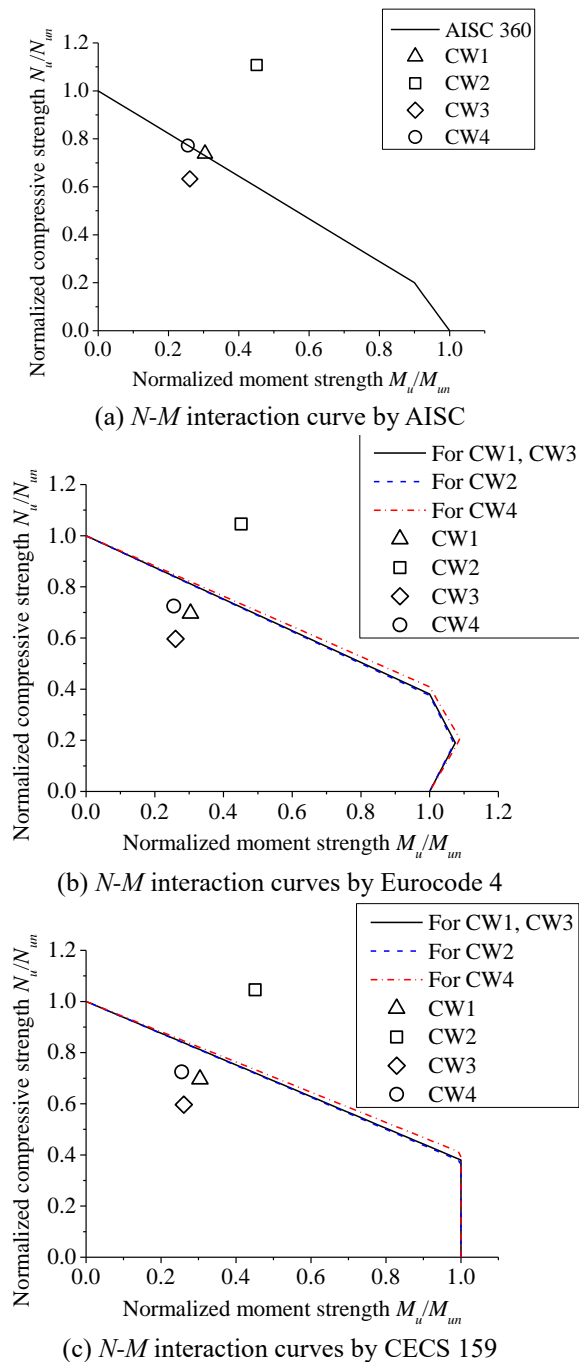


Fig. 16 Comparison between test data and modern codes

Acknowledgments

This work is sponsored by the Natural Science Foundation of Jiangsu Province (Grant No. BK20170685), and the National Key Research and Development Program of China (Grant No. 2017YFC0703802). The authors would like to thank the Zhejiang Southeast Space Frame Group Company Limited for the supply of test specimens, Jianhong Han in the steel research group for the help with test preparation, and Xiongliang Zhou, Weigang Chen, Yunfei He and Jianwei Ni for their assistance with the specimen fabrication.

References

- AISC 360-16 (2016), Specification for structural steel buildings, American Institute of Steel Construction; Chicago, USA.
- Bafti, F.G., Mortezaei, A. and Kheyroddin, A. (2019), "The length of plastic hinge area in the flanged reinforced concrete shear walls subjected to earthquake ground motions", *Struct. Eng. Mech.*, **69** (6), 651-665. <https://doi.org/10.12989/sem.2019.69.6.651>.
- Beiraghi, H. (2018), "Energy demands in reinforced concrete wall piers coupled by buckling restrained braces subjected to near-fault earthquake", *Steel Compos. Struct.*, **27**(6), 703-716. <http://dx.doi.org/10.12989/scs.2018.27.6.703>.
- Bruhl, J.C. and Varma, A.H. (2018), "Experimental evaluation of steel-plate composite walls subject to blast loads", *J. Struct. Eng.*, **144**(9), 04018155. [http://dx.doi.org/10.1061/\(ASCE\)ST.1943-541X.0002163](http://dx.doi.org/10.1061/(ASCE)ST.1943-541X.0002163).
- CECS 159:2004 (2004), Technical specification for structures with concrete-filled rectangular steel tube members, China Association for Engineering Construction Standardization; Beijing, China.
- Chen, L., Mahmoud, H., Tong, S.M. and Zhou, Y. (2015), "Seismic behavior of double steel plate-HSC composite walls", *Eng. Struct.*, **102**, 1-12. <http://dx.doi.org/10.1016/j.engstruct.2015.08.017>.
- Chen, L.H., Wang, S.Y., Lou, Y. and Xia, D.R. (2019), "Seismic behavior of double-skin composite wall with L-shaped and C-shaped connectors", *J. Constr. Steel Res.*, **160**, 255-270. <http://dx.doi.org/10.1016/j.jcsr.2019.05.033>.
- Curkovic, I., Skejic, D. and Dzeba, I. (2019), "Seismic performance of steel plate shear walls with variable column flexural stiffness", *Steel Compos. Struct.*, **33**(1), 833-850. <http://dx.doi.org/10.12989/scs.2019.33.1.833>.
- Deng, E.F., Zong, L. and Ding, Y. (2019), "Numerical and analytical study on initial stiffness of corrugated steel plate shear walls in modular construction", *Steel Compos. Struct.*, **32**(3), 347-359. <http://dx.doi.org/10.12989/scs.2019.32.3.347>.
- EN 1994-1-1:2004 (2004), Eurocode 4: Design of composite steel and concrete structures-Part 1-1: General rules and rules for buildings. British Standards Institution; London, UK.
- Eom, T.S., Park, H.G., Lee, C.H., Kim, J.H. and Chang, I.H. (2009), "Behavior of double skin composite wall subjected to in-plane cyclic loading", *J. Struct. Eng.*, **135**(10), 1239-1249. [http://dx.doi.org/10.1061/\(ASCE\)ST.1943-541X.0000057](http://dx.doi.org/10.1061/(ASCE)ST.1943-541X.0000057).
- GB 50010-2010 (2015), Code for design of concrete structures, China Architecture & Building Press, Beijing, China.
- GB/T 2975-2018 (2018), Steel and Steel Products-Location and Preparation of Samples and Test Pieces for Mechanical Testing, China Standards Press, Beijing, China.
- GB/T 50081-2019 (2019), Standard for test methods of concrete physical and mechanical properties, China Architecture &

- Building Press, Beijing, China.
- Hilo, S.J., Badaruzzaman, W.H.W, Osman, S.A. and Al-Zand, A.W. (2016), "Structural behavior of composite wall systems strengthened with embedded cold-formed steel tube", *Thin Wall Struct.*, **98**, 607-616. <http://dx.doi.org/10.1016/j.tws.2015.10.028>.
- Hossain, K.M.A., Mol, L.K. and Anwar, M.S. (2015), "Axial load behaviour of pierced profiled composite walls with strength enhancement devices", *J. Constr. Steel Res.*, **110**, 48-64. <http://dx.doi.org/10.1016/j.jcsr.2015.03.009>.
- Hu, H.S., Nie, J.G. and Eatherton, M.R. (2014), "Deformation capacity of concrete-filled steel plate composite shear walls", *J. Constr. Steel Res.*, **103**, 148-158. <http://dx.doi.org/10.1016/j.jcsr.2014.08.006>.
- Huang, S.T., Huang, Y.S., He, A., Tang, X.L., Chen, Q.J., Liu, X. and Cai, J. (2018), "Experimental study on seismic behaviour of an innovative composite shear wall", *J. Constr. Steel Res.*, **148**, 165-179. <https://doi.org/10.1016/j.jcsr.2018.05.003>.
- Huang, Z. and Liew, J.Y.R. (2016), "Compressive resistance of steel-concrete-steel sandwich composite walls with J-hook connectors", *J. Constr. Steel Res.*, **124**, 142-162. <http://dx.doi.org/10.1016/j.jcsr.2016.05.001>.
- Ji, X.D., Cheng, X.W., Jia, X.F. and Varma, A.H. (2017), "Cyclic in-plane shear behavior of double-skin composite walls in high-rise buildings", *J. Struct. Eng.*, **143**(6), 04017025. [https://doi.org/10.1061/\(ASCE\)ST.1943-541X.0001749](https://doi.org/10.1061/(ASCE)ST.1943-541X.0001749).
- Keihani, R., Bahadori-Jahromi, A. and Goodchild, C. (2019), "The significance of removing shear walls in existing low-rise RC frame buildings - Sustainable approach", *Struct. Eng. Mech.*, **71**(5), 563-576. <https://doi.org/10.12989/sem.2019.71.5.563>.
- Liu, W.Y., Li, G.Q. and Jiang, J. (2018), "Capacity design of boundary elements of beam-connected buckling restrained steel plate shear wall", *Steel Compos. Struct.*, **29**(2), 231-242. <https://doi.org/10.12989/scs.2018.29.2.231>.
- Ma, K., Ma, Y. and Liu, B. (2019), "Seismic behavior of double steel concrete composite walls", *Struct. Design Tall Spec. Build.*, **28**, e1623. <https://doi.org/10.1002/tal.1623>.
- Nguyen, N.H. and Whittaker, A.S. (2017), "Numerical modelling of steel-plate concrete composite shear walls", *Eng. Struct.*, **150**, 1-11. <http://dx.doi.org/10.1016/j.engstruct.2017.06.030>.
- Nie, J.G., Hu, H.S., Fan, J.S., Tao, M.X., Li, S.Y. and Liu, F.J. (2013), "Experimental study on seismic behavior of high-strength concrete filled double-steel-plate composite walls", *J. Constr. Steel Res.*, **88**, 206-219. <http://dx.doi.org/10.1016/j.jcsr.2013.05.001>.
- Prabha, P., Marimuthu, V., Saravanan, M., Palani, G.S., Lakshmanan, N. and Senthil, R. (2013), "Effect of confinement on steel-concrete composite light-weight load-bearing wall panels under compression", *J. Constr. Steel Res.*, **81**, 11-19. <http://dx.doi.org/10.1016/j.jcsr.2012.10.008>.
- Qin, Y., Shu, G.P., Du, E.F. and Lu, R.H. (2018), "Buckling analysis of elastically-restrained steel plates under eccentric compression", *Steel Compos. Struct.*, **29**(3), 379-389. <https://doi.org/10.12989/scs.2018.29.3.379>.
- Qin, Y., Shu, G.P., Zhou, G.G. and Han, J.H. (2019), "Compressive behavior of double skin composite wall with different plate thicknesses", *J. Constr. Steel Res.*, **157**, 297-313. <https://doi.org/10.1016/j.jcsr.2019.02.023>.
- Qin, Y., Shu, G.P., Zhou, X.L., Han, J.H. and Zhang, H.K. (2020), "Behavior of T-shaped sandwich composite walls with truss connectors under eccentric compression", *J. Constr. Steel Res.*, **169**, 106067. <https://doi.org/10.1016/j.jcsr.2020.106067>.
- Seddighi, M., Barkhordari, M.A. and Hosseinzadeh, S.A.A. (2019), "Behavior of FRP-reinforced steel plate shear walls with various reinforcement designs", *Steel Compos. Struct.*, **33**(5), 729-746. <http://dx.doi.org/10.12989/scs.2019.33.5.729>.
- Sener, K.C., Varma, A.H., and Ayhan, D. (2015), "Steel-plate composite (SC) walls: Out-of-plane flexural behavior, database, and design", *J. Constr. Steel Res.*, **108**, 46-59. <http://dx.doi.org/10.1016/j.jcsr.2015.02.002>.
- Shariati, M., Faegh, S.S., Mehrabi, P., Bahavarnia, S., Zandi, Y., Masoom, D.R., Togholi, A., Trung, N.T. and Salih, M.N.A. (2019), "Numerical study on the structural performance of corrugated low yield point steel plate shear walls with circular openings", *Steel Compos. Struct.*, **33**(4), 569-581. <http://dx.doi.org/10.12989/scs.2019.33.4.569>.
- Wei, F., Zheng, Z., Yu, J. and Wang, Y. (2019), "Structure behavior of concrete filled double-steel-plate composite walls under fire", *Adv. Struct. Eng.*, **22**(8), 1895-1908. <https://doi.org/10.1177/1369433218825238>.
- Xiong, Q., Chen, Z., Zhang, W., Du, Y., Zhou, T. and Kang, J. (2017), "Compressive behaviour and design of L-shaped columns fabricated using concrete-filled steel tubes", *Eng. Struct.*, **152**, 758-770. <https://doi.org/10.1016/j.engstruct.2017.09.046>.
- Yan, J.B., Wang, Z., Wang, T. and Wang, X.T. (2018), "Shear and tensile behaviors of headed stud connectors in double skin composite shear wall", *Steel Compos. Struct.*, **26**(6), 759-769. <https://doi.org/10.12989/scs.2013.91.4.1301>.
- Yan, J.B., Chen, A.Z. and Wang, T. (2019), "Developments of double skin composite walls using novel enhanced C-channel connectors", *Steel Compos. Struct.*, **33**(6), 877-889. <https://doi.org/10.12989/scs.2019.33.6.877>.
- Yang, Y., Liu, J.B. and Fan, J.S. (2016), "Buckling behavior of double-skin composite walls: An experimental and modeling study", *J. Constr. Steel Res.*, **121**, 126-135. <http://dx.doi.org/10.1016/j.jcsr.2016.01.019>.
- Yuksel, S.B. (2019), "Experimental investigation of retrofitted shear walls reinforced with welded wire mesh fabric", *Struct. Eng. Mech.*, **70**(2), 133-141. <https://doi.org/10.12989/sem.2019.70.2.133>.
- Zhang, K., Varma, A.H., Malushte, S.R. and Gallocher, S. (2014), "Effect of shear connectors on local buckling and composite action in steel concrete composite walls", *Nucl. Eng. Des.*, **269**, 231-239. <http://dx.doi.org/10.1016/j.nucengdes.2013.08.035>.

DL